Design and Motion Planning of a Two-Module Collaborative Indoor Pipeline Inspection Robot

Young-Sik Kwon, *Member, IEEE*, and Byung-Ju Yi, *Member, IEEE*

Abstract—This paper deals with a design and motion planning algorithm of a caterpillar-based pipeline robot that can be used for inspection of 80–100-mm pipelines in an indoor pipeline environment. The robot system uses a differential drive to steer the robot and spring loaded four-bar mechanisms to assure that the robot expands to grip the pipe walls. Unique features of this robot are the caterpillar wheels, the analysis of the four-bar mechanism supporting the treads, a closed-form kinematic approach, and an intuitive user interface. In addition, a new motion planning approach is proposed, which uses springs to interconnect two robot modules and allows the modules to cooperatively navigate through difficult segments of the pipes. Furthermore, an analysis method of selecting optimal compliance to assure functionality and cooperation is suggested. Simulation and experimental results are used throughout the paper to highlight algorithms and approaches.

Index Terms—Caterpillar wheel, inspection robot, kinematics, optimal design, pipeline robot, reconfigurable.

I. INTRODUCTION

RECENTLY, many pipeline inspection robot systems have been developed. Development of pipeline robots began for inspecting large pipelines ranging from 100 to 300 mm. These pipelines are commonly used in manufacturing sites as sewer pipes and gas and oil pipelines. They are also used in nuclear power plants. Pipeline inspection robot systems improve safety and reduce work time.

In-pipe robots can be classified into several elementary forms according to movement patterns. Wheel-type pipeline inspection robots are popular and have been investigated in the laboratory. Oya and Okada [1] developed a flat-type pipeline robot. Hirose *et al.* [2] proposed several types of pipeline inspection robots ranging from Φ25, Φ50, up to Φ150 pipes. Jun *et al.* [3] proposed a robot that has six-wheeled driving arms fixed circumferentially 60° apart on the robot body frame. Roh and Choi [4]

developed underground urban gas pipeline robots with a miniature differential-drive chassis using wheels. However, not all of these wheel robots can pass through elbows or T-branches with a small radius of curvature.

Inchworm-type mechanisms are suitable for pipelines with a diameter smaller than 30 mm. Fukuda *et al.* [5] studied rubber actuators for a pipeline inspection robot. Bertetto and Ruggiu [6] developed an in-pipe inchworm pneumatic flexible robot. However, these were not effective because of their low speed and poor reliability.

The inchworm robot is similar to the snake-like robot. Transeth and Pettersen [7] suggest a nonsmooth mathematical model for wheel-less snake robots, which allows the snake robot to push against external obstacles apart from a flat ground. Crespi and Ijespeert [8] developed an amphibious snake robot. They have presented various experiments with a real robot and in simulation: swimming, crawling on horizontal ground, and crawling on slopes. Hirose and Yamada [9] introduced many types of snake-like robots. Snake-like robots use a number of active joints or modules; thus, their development cost is expensive and they need more energy for operation.

Crawler-type robot mechanisms are able to adapt to changes in the pipeline's environment. Usually, crawler-type robots use a caterpillar wheel. With this type, it is easy to inspect a collapsed part or choked part of a pipeline. The robot may have a large traction force because of its wide contact area. Kim [10] developed the fully autonomous mobile pipeline exploration robot to explore pipeline structures autonomously. Its performance has been evaluated. Park *et al.* [11] proposed an in-pipe robot that is adaptable to pipe diameters from 400 to 700 mm. Raytheon [12] developed a multidimensional mobility robot. Crawler robot mechanisms are difficult to make in small sizes.

The cleanliness of indoor pipelines for water supply in a home or office is directly related to public health. Goods are affected by the cleanliness of industrial water and liquid material. In order to perform inspection tasks in indoor pipelines and small industrial indoor pipelines, an inspection robot must work for pipe diameters less than 100 mm with multiple T-branches or elbows. The design of such a robot is challenging; many components of pipeline inspection robot systems, such as a robot mechanism, a communication system, a power supply, and a user interface, must be packaged in a small volume. Furthermore, indoor pipelines have a more complex geometry than do outdoor pipelines.

Previously developed pipeline robot systems have been tested on straight, slightly inclined, or simply curved pipelines, because the task space of the developed robot is primarily in sewer, gas, and oil pipelines. Navigation through a pipeline with multiple curves or T-branches remains a difficult problem. Some types

of robots are equipped with an active joint [2], [9], [13], [15] or active universal joint [14] to overcome difficult motion at a T-branch or an elbow, but they are too big to apply to indoor pipelines and too expensive to make. Raytheon [12] uses active joints to couple the modules (which gives improved climbing capability). Roh and Choi [4] initially discussed motion planning algorithms of pipeline robots by using an active steering method and a differential-driven method. What has not yet been completed is a closed-form kinematic model for a pipeline robot with three powered wheel chains.

In a pipeline, the radii of pipes vary by the usage and flow conditions of the facility. There are two types of adaptation mechanisms to overcome the pipeline's environment such as active linkage types and passive linkage types. Active linkage systems use actuators to control the normal force on the contact parts actively [11]. However, they need more space to install an actuator, and the cost to manufacture the robot is more. Passive linkage system is designed with elastic components without actuators. They can adapt to wide ranges of diameter with simple structures. Most of the related works [1]–[4], [11], [12] used one compliant spring in the main axis of the pipeline robot. Thus, an irregular surface at one spot may cause deflection of the whole body rather than a local deflection.

In addition, a spring coupling of two robot modules or more [2], [9], [12] has been used in pipeline robots, but they were not used for the motion planning of two robots. Kimura *et al.* [19] developed Genbu, which is categorized as active-wheel passive-joint articulated mobile robots. The passive joint is 2 degrees of freedom (DOF) (prismatic and revolution) and it contains two sensors to check the state of Genbu (three types of stuck conditions). It is a good application of the compliant coupling between robot modules, but it is not designed for the motion planning of robots.

Zhang *et al.* [20] designed a flexible squirm pipe robot. It has a flexible axle and a self-steering device. All the functions of this robot are realized only by one motor; therefore, the robot has a simple structure and high motor usage. It is similar to our robot in so far as it uses collaboration between two modules and flexible link parts (axle); however, this robot mechanism needs an active steering device controlled by four rods. This means the robot needs more actuators.

Kim and Minor [22] presented a kinematic motion control strategy for an *n*-axle compliant framed modular wheeled mobile robot. This robot is essentially a passive-joint active-wheel snake robot that coordinates motion of the robot modules and is critical for maximizing mobility and minimizing traction forces.

In this paper, we introduce a crawler-type pipeline inspection robot that is designed to inspect 80–100-mm-diameter pipelines that are appropriate for inspection and navigation of indoor pipelines and small industrial indoor pipelines. Contributions of this paper are suggestion of a closed-form kinematic model of the pipeline inspection robot, a new motion planning algorithm using springs to allow the robot modules to cooperatively navigate through difficult segments of the pipes, and the analysis method of selecting optimal compliance to assure functionality and cooperation.
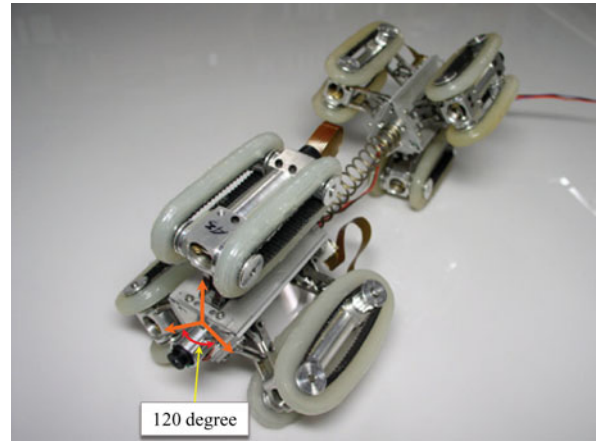

Fig. 1.   Whole view of the collaboration-type pipeline inspection robot.

The structure of this paper is as follows. Section II presents the characteristics of the pipeline robot. In Section III, we present a closed-form kinematic model of the pipeline inspection robot driven by three powered caterpillar wheel chains (CWCs). An analytic Jacobian is derived, and the optimal value of the radius of the robot wheel is found by using two kinematic indices in Section IV. In Section V, a static force analysis is performed for actuator sizing. This result is applied to determine the specification of the compression spring embedded in the foldable four-bar mechanism. In Section VI, motion planning algorithms for the pipeline robot are proposed. Specifically, cooperation between two robots contributes to avoiding singular motion in a special situation and resulting successful navigation of the robots through the pipeline. Actual implementation and its experimental results are shown in Sections VII and VIII, respectively. Finally, we draw conclusions in Section IX.

II. CHARACTERISTICS OF ROBOT

A. Structure

The robot that is shown in Fig. 1 consists of two robot modules connected by a compressive spring. Each robot module consists of a main body, three linkage structures, and three caterpillar wheels as shown in Fig. 2.

The body is constructed as a triangle, which is adequate to support the three linkage structures. For each chain, two four-bar linkage structures that are similar to scissors connect the wheel mechanism to the hinges of the main body. The hinge holders are connected by a spring shaft. The deflection of the compression spring allows foldable characteristics of the linkage structure so that the caterpillar wheel adjusts itself to the inner wall of the pipeline with a slight change of its diameter.

A micro-dc motor that is equipped with an encoder is enclosed inside the caterpillar wheel of diameter 10 mm. The encoder measures the moving distance of the robot. In the wheel mechanism, the driving power is transmitted to the wheel by a set of bevel gears, a pulley, and a belt, as shown in Fig. 2.

Kuwada *et al.* [21] developed a snake-like robot for 3-D pipelines. Their robot consisted of 13 actuators and applied a
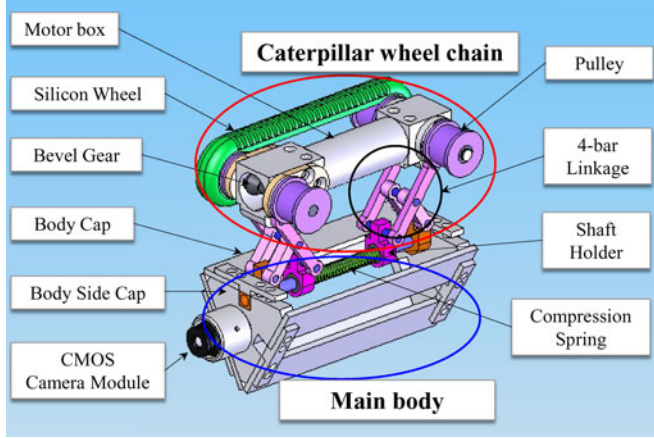
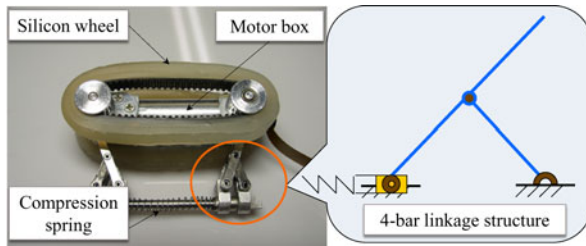Fig. 2. Linkage structure and caterpillar wheel module.

Fig. 3. Silicon caterpillar wheel and four-bar linkage structure.

sinusoidal wave drive that made the robot form sinusoidal waves to obtain the propelling force needed to grip the pipe walls. To increase the gripping force and the propelling force, the silicone rubber covers were attached on the links. In our mechanism, we used silicone caterpillar wheels to increase the gripping force and the propelling force.

The caterpillar wheel that is shown in Fig. 3 is made of a bevel gear set and a wrapping silicon belt. Caterpillar wheel modules are arranged 120° apart. Thus, the robot is able to hold the surface of the pipeline firmly while moving on the surface of the pipeline very smoothly. Since each caterpillar is controlled independently, it is possible to perform steering at elbows or T-branches of pipelines by differentiating the velocities of the three wheels.

B. Advantage of the Caterpillar Wheel

This robot was designed to pass through multiple elbows or T-branches using the CWC. A regular wheel mechanism cannot work properly in the pipeline with a small radius of curvature as shown in Fig. 4(b) because, sometimes, the wheels lose contact with the surface. However, a caterpillar wheel works properly because all CWCs maintain contact with the surface of the pipeline as shown in Fig. 4(a). The robot works stably as each CWC works independently even when there are some irregular surfaces inside the pipeline. As illustrated in Fig. 5, if one of the three CWCs contacts a collapsed part or a choked part of the pipeline, then only the corresponding CWC will be folded and adjust itself to the choked part. However, the other CWCs are not influenced. In video clip 1, a dynamic simula-
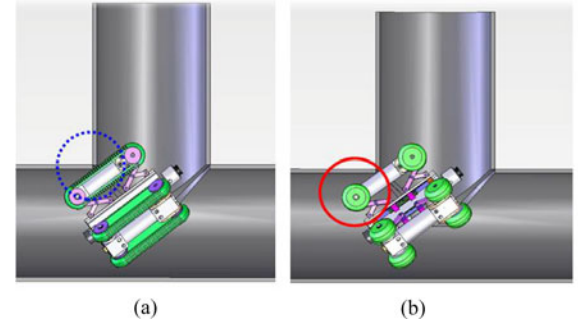

Fig. 4. Comparison of caterpillar and regular wheels. (a) Caterpillar wheel goes through the T-branch, and (b) regular wheel does not go through the T-branch.
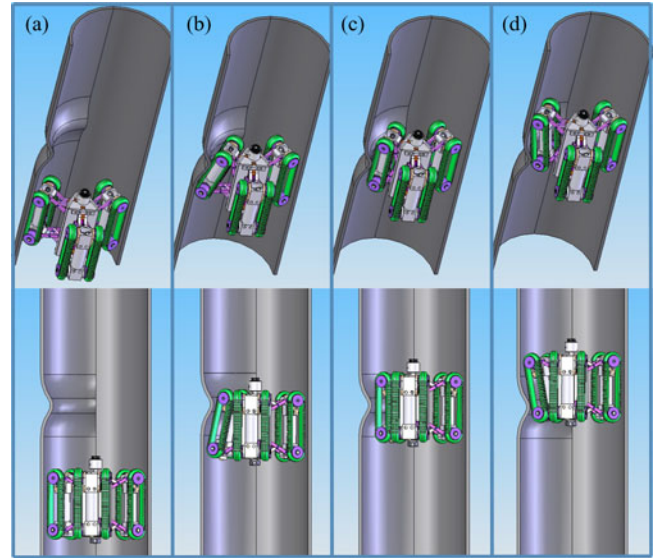

Fig. 5. Adaptability of the caterpillar wheel. (a) Robot approaches the choked section, (b) one wheel chain contacts the choked part, (c) the wheel chain deflects, and (d) the wheel goes through the choked area.

tion using commercially available software (DAFUL made by Virtual Motion Co.) is performed to show the movement of the robot through a choked part of the pipeline.

C. Specification of the Single-Module Robot

Table I shows the specification of the robot. The length of the robot module is 78 mm, and the exterior diameter increases from 80 up to 100 mm. The total length of the robot device (including two robot modules and a compression spring) is 230 mm. The weight of each robot is 266 g.

III. KINEMATIC MODELING OF THE PIPELINE INSPECTION ROBOT

A. Mobility Analysis

Mobility is the number of minimum input parameters that are required to specify all of the locations of the system relative to another. The mobility of the robot is one when it moves in a straight pipeline. However, the robot has two additional

TABLE I
SPECIFICATION OF THE ROBOT

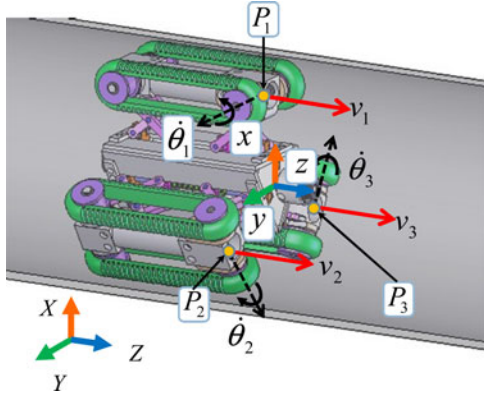| Specification	Value
Weight of each robot module	266 g
Motor diameter	10 mm
Length of the robot module	78 mm
Total length of the robot	230 mm
Exterior diameter	80-100 mm
Max traction force of the robot module	1.183 Nm
Linear speed	5.5 cm/sec
Max. speed	9 cm/sec
Camera and sensor module length	18 mm
Serial communication distance	15 M

Fig. 6.   Whole view of the pipeline inspection robot.

Fig. 7. $v_1 = v_2 = v_3$. (a) Cross-sectional view of the pipeline. (b) Velocity profile at the side view of the pipeline.

mobilities when steering at elbows or T-branches. Specially, at a T-branch, the instantaneous motion of this robot can be modeled as the translation along the pipeline and two rotations about the axes orthogonal to the direction of motion of the robot. Thus, these three DOF can be controlled by three actuators, one for each chain.

B. Kinematics

In this section, we derive the kinematic model of the inspection robot given in Fig. 6. The detailed structure, the coordinate system, the joint variables, and parameters of this mechanism are given in Figs. 6 and 7. XYZ represents the global reference frame, and xyz denotes the local coordinate frame attached to the center of the pipeline inspection robot; $\hat{i}$, $\hat{j}$, and $\hat{k}$ are the unit vectors of the local coordinate frame. The x-axis always points to P_1 no matter how the robot moves.

First, we assume that every caterpillar wheel retains a line contact at the inner wall of the pipeline, and that the wheel does not slip in the horizontal direction and does not rotate about the z-axis, but is allowed to move along the z-axis. The power generated by the mounted micromotor is transmitted to the caterpillar wheel through a bevel gear. We define θ_1, θ_2, and θ_3 as the rotating angles of the caterpillar wheels; r denotes the radius of the wheel, and a denotes the radius of the robot body. Then, the linear velocities v_1, v_2, and v_3 at the center of the wheels are given by
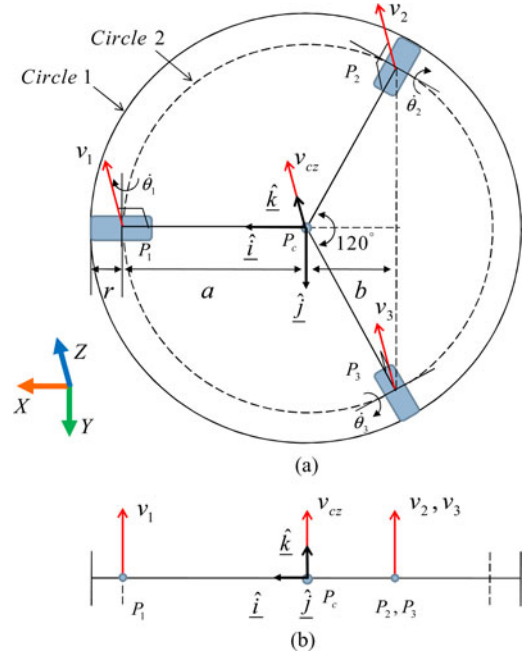
$$v_1 = r\dot{\theta}_1$$

$$v_2 = r\dot{\theta}_2$$

$$v_3 = r\dot{\theta}_3. \tag{1}$$

In general, the linear velocities v_1, v_2, and v_3 have different magnitudes at elbows or T-branches. Then, the linear velocity at the center P_c of the robot is denoted as v_{cz}, and the rotational velocities about the body fixed axes $\hat{i}$ and $\hat{j}$ are denoted as ω_x and ω_y. Then, in order to derive the kinematic relationship between the input velocity ($\dot{\theta}_1$, $\dot{\theta}_2$, and $\dot{\theta}_3$) and the output velocity (ω_x, ω_y, and v_{cz}), we analyze the components of the output velocity for four cases. Fig. 7(a) and (b) shows the cross-sectional view of the pipeline and the velocity profile at the side view of the pipeline, respectively.

Case 1 ($v_1 = v_2 = v_3$): Case 1 is the state in which the robot moves in the straight pipeline. As shown in Fig. 7(a), the three wheels' velocities are equal; thus, the linear velocity v_{cz} at the center can be described as

$$v_{cz} = v_1(= v_2 = v_3). \tag{2}$$

However, the rotational velocities ω_x and ω_y do not exist.

Case 2 (Only One Velocity Exists (v_1)): Case 2 is the state where only one velocity exists, as shown in Fig. 8. In this case, the points P_2 and P_3 are stationary, and at the point P_1, a linear velocity v_1 is generated. Then, the linear velocity at the center P_c of the robot is obtained by geometric analysis. Resultantly, the robot rotates about the line $\overline{P_2 P_3}$ with the rotational velocity ω_1 given by

$$\omega_1 = \frac{v_1}{a+b}. \tag{3}$$

Since $b = a\cos 60°$, (3) becomes

$$\omega_1 = \frac{v_1}{1.5a}. \tag{4}$$

Fig. 8. v_1 exists. (a) Cross-sectional view of the pipeline. (b) Velocity profile at the side view of the pipeline.

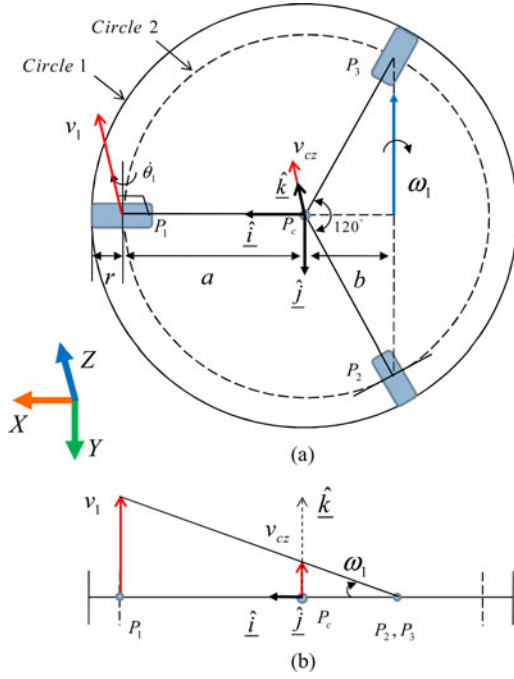Fig. 9. v_1 and v_2 exist. (a) Cross-sectional view of the pipeline. (b) Velocity profile at the side view of the pipeline.

The linear velocity v_1 is generated by rotation of the caterpillar wheel, which can be described as

$$v_1 = r\dot{\theta}_1. \tag{5}$$

At this time, the rotational velocity vector $\underline{\omega}_1$ with respect to the local coordinate fixed to the robot can be expressed as

$$\underline{\omega}_1 = -\frac{r}{1.5a}\dot{\theta}_1. \tag{6}$$

Then, the components of $\underline{\omega}_1$ are denoted as

$$\omega_x = 0 \tag{7}$$

and

$$\omega_y = -\frac{r}{1.5a}\dot{\theta}_1. \tag{8}$$

Now, the linear velocity v_{cz} at the center of the robot is obtained from (1) and the triangular geometry of Fig. 8(b) as

$$v_{cz} = \frac{b}{a+b}v_1 = \frac{0.5a}{1.5a}v_1 = \frac{r}{3}\dot{\theta}_1. \tag{9}$$

Case 3 (Two Velocities Exist (v_1, v_2)): Case 3 is the state in which two velocities exist, as shown in Fig. 9. In this case, the point P_3 is stationary, and at the points P_1 and P_2, the linear velocities v_1 and v_2 are generated. Then, the linear velocity at the center P_c of the robot is obtained by geometric analysis. Resultantly, the rotation velocity ω_{12} is generated by the linear velocity v_1 and v_2. Fig. 9(a) shows that when the linear velocities v_1 and v_2 are the same, the rotational velocity $\underline{\omega}_{12}$ is given by

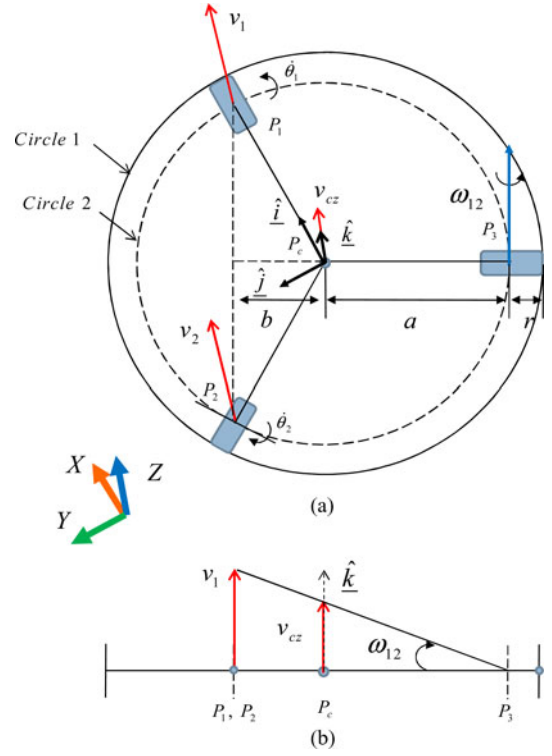$$\underline{\omega}_{12} = \frac{v_1}{a+b} = \frac{v_1}{1.5a}. \tag{10}$$

The rotational velocity vector $\underline{\omega}_{12}$ with respect to the local coordinate fixed to the robot can be described by

$$\underline{\omega}_{12} = \frac{r\dot{\theta}_2}{1.5a}(\cos 30°\hat{\underline{i}} - \sin 30°\hat{\underline{j}}) = \frac{\sqrt{3}r}{3a}\dot{\theta}_2\hat{\underline{i}} - \frac{r}{3a}\dot{\theta}_2\hat{\underline{j}} \tag{11}$$

where $\omega_x = (\sqrt{3}r/3a)\dot{\theta}_2$ and $\omega_{\bar{y}} = -(r/3a)\dot{\theta}_2$.

In this case, the robot rotates about the line passing through the point P_3. The linear velocity v_{cz} at the center of the robot is obtained geometrically as

$$v_{cz} = \frac{a}{a+b}v_1 = \frac{a}{1.5a}v_1 = \frac{2r}{3}\dot{\theta}_1 \text{ or } \frac{2r}{3}\dot{\theta}_2. \tag{12}$$

Case 4 ($v_1 \neq v_2 \neq v_3$): Case 4 is the state where three velocities coexist with different values (e.g., $v_3 < v_2 < v_1$), as shown in Fig. 10. In this case, the rotational velocity vector of the robot is equal to the summation of the rotational velocity vector created by the linear velocity of each wheel. That is to say, when only v_1 exists, the rotational velocity vector is identical to (6). Similarly, when only v_2 exists, the rotational velocity vector is as follows:

$$\underline{\omega}_2 = \frac{r\dot{\theta}_2}{1.5a}(\cos 30°\hat{\underline{i}} + \sin 30°\hat{\underline{j}}) = \frac{\sqrt{3}r}{3a}\dot{\theta}_2\hat{\underline{i}} + \frac{r}{3a}\dot{\theta}_2\hat{\underline{j}}, \tag{13}$$

where $\omega_x = (\sqrt{3}r/3a)\dot{\theta}_2$, and $\omega_y = (r/3a)\dot{\theta}_2$.
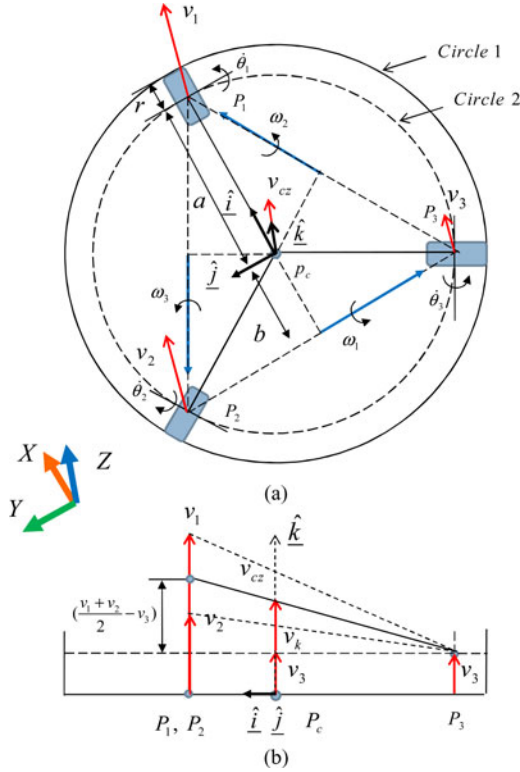
Fig. 10. v_1, v_2, and v_3 exist. (a) Cross-sectional view of the pipeline. (b) Velocity profile at the side view of the pipeline.

In addition, when only v_3 exists, the rotational velocity vector is as follows:

$$\underline{\omega}_2 = \frac{r\dot{\theta}_3}{1.5a}(-\cos 30°\hat{\underline{i}} + \sin 30°\hat{\underline{j}})$$

$$= -\frac{\sqrt{3}r}{3a}\dot{\theta}_3\hat{\underline{i}} + \frac{r}{3a}\dot{\theta}_3\hat{\underline{j}}, \tag{14}$$

where $\omega_x = -(\sqrt{3}r/3a)\dot{\theta}_3$, and $\omega_y = (r/3a)\dot{\theta}_3$.

Assuming that v_1, v_2, and v_3 exist at the same time, the total rotational velocity vector of the robot is formed by summation of (6), (13), and (14):

$$\underline{\omega} = \omega_x\hat{\underline{i}} + \omega_y\hat{\underline{j}} \tag{15}$$

where

$$\omega_x = \frac{\sqrt{3}r}{3a}\dot{\theta}_2 - \frac{\sqrt{3}r}{3a}\dot{\theta}_3 \tag{16}$$

and

$$\omega_y = -\frac{2r}{3a}\dot{\theta}_1 + \frac{r}{3a}\dot{\theta}_2 + \frac{r}{3a}\dot{\theta}_3. \tag{17}$$

Now, the linear velocity v_{cz} at the center of the robot is obtained by taking the average of v_1, v_2, and v_3 as

$$v_{cz} = \frac{1}{3}(v_1 + v_2 + v_3) = \frac{r}{3}(\dot{\theta}_1 + \dot{\theta}_2 + \dot{\theta}_3). \tag{18}$$

Finally, the relationship between the input velocity vector $\underline{\dot{\theta}}_a = (\dot{\theta}_1 \ \dot{\theta}_2 \ \dot{\theta}_3)^T$ and the output velocity vector $\underline{\dot{u}} = (\omega_x \ \omega_y \ v_{cz})^T$ is constructed as

$$\underline{\dot{u}} = [G_a^u]\underline{\dot{\theta}}_a \tag{19}$$

by combining (15) and (18). Here, the Jacobian is given as

$$[G_a^u] = \begin{bmatrix} 0 & \dfrac{\sqrt{3}r}{3a} & -\dfrac{\sqrt{3}r}{3a} \\[2mm] -\dfrac{2r}{3a} & \dfrac{r}{3a} & \dfrac{r}{3a} \\[2mm] \dfrac{r}{3} & \dfrac{r}{3} & \dfrac{r}{3} \end{bmatrix}. \tag{20}$$

If the robot body rotates by θ_c about the local z-axis, then the rotational parts of the Jacobian given by (21) contain the θ_c term. The angle θ_c can be measured by a single-axis gyro sensor and a dual-axis accelerometer installed in the real robot

$$[G_a^u] = \begin{bmatrix} \dfrac{2r\sin\theta_c}{3a} & \left(\dfrac{\sqrt{3}r\cos\theta_c}{3a} - \dfrac{r\sin\theta_c}{3a}\right) \\[3mm] -\dfrac{2r\cos\theta_c}{3a} & \left(\dfrac{\sqrt{3}r\sin\theta_c}{3a} + \dfrac{r\cos\theta_c}{3a}\right) \\[3mm] \dfrac{r}{3} & \dfrac{r}{3} \end{bmatrix}$$

$$\begin{matrix} -\left(\dfrac{\sqrt{3}r\cos\theta_c}{3a} + \dfrac{r\sin\theta_c}{3a}\right) \\[3mm] -\left(\dfrac{\sqrt{3}r\sin\theta_c}{3a} - \dfrac{r\cos\theta_c}{3a}\right) \\[3mm] \dfrac{r}{3} \end{matrix} \tag{21}$$

There is no prior work addressing the analytic Jacobian model of in-pipe robots. It is useful in the design of a robotic system, as well as in the analysis of robot performance.

For a given linear velocity (v_{cz}) and rotational velocities (ω_x and ω_y) at the center of the robot, the angular velocity of the wheels are calculated as

$$\underline{\dot{\theta}}_a = [G_a^u]^{-1}\underline{\dot{u}}. \tag{22}$$

The rotation angle of each wheel is obtained by numerical integration of (22).

IV. OPTIMAL DESIGN

In this section, optimal kinematic parameterization of the robot is conducted through singular value analysis of $[G_a^u]$. An equality constraint exists in this analysis. The diameter of the pipeline is set as a constant value, which creates the following constraint equation relating a and r:

$$2(a + r) = D \tag{23}$$

where a and r are defined in Fig. 7, and D denotes the inner diameter of the pipeline.

Denoting $\sigma_{\max}$ and $\sigma_{\min}$ as the maximum and minimum singular values of the Jacobian, the isotropy index is expressed as

$$\sigma_I = \frac{\sigma_{\min}}{\sigma_{\max}}. \tag{24}$$

Here, large σ_I implies an isotropic motion capability in every direction.
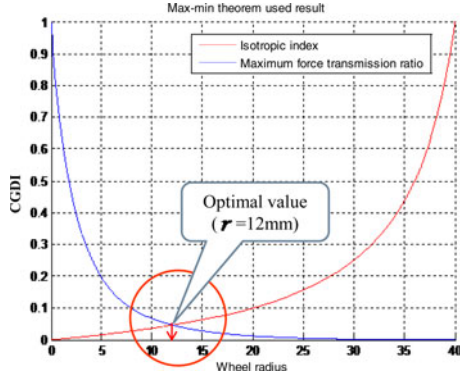
Fig. 11. Optimal value of the radius.

Fig. 12. Phase of wheel angular velocity. (a) Change in the joystick direction (angle) θ_J. (b) $\omega_x = 15\,°/\text{s}$, $v_{cz} = 3\,\text{cm/s}$.

The maximum force transmission ratio is defined as the operational load created by one unit magnitude of the input load. It is defined as (refer to the Appendix)

$$\sigma_f = \frac{1}{\sigma_{\min}}. \tag{25}$$

The greater σ_f, the larger the operational load.

After normalizing the two indices, we combine them as a composite global design index (CGDI) given by

$$\text{CGDI} = \min\{\tilde{\sigma}_I^\alpha, \tilde{\sigma}_F^\beta\} \tag{26}$$

which is defined as the minimum value of the aforementioned design indices at a set of design parameters [17]. In (26), α and β denote the weighting factor for the isotropy index and the maximum force transmission ratio, respectively.

Usually, a large value implies large weighting. In order to evenly satisfy the several design objectives for all design indices, all of the weighting factors are set to 1. Otherwise, different values should be selected. Now, a set of optimal design parameters is chosen as the set with the maximum CGDI among all CGDIs calculated for all sets of design parameters.

In the design of the pipeline robot, the traction force of the robot is more important than the speed of the robot, since the robot should always sustain its own weight under gravity. Thus, we give more weighting to the maximum force transmission ratio to maximize the payload rather than increasing the speed of the robot (i.e., the weighting factor α for σ_I is 1, and the weighting factor β for σ_f is 2). Fig. 11 shows CGDI with respect to the radius of the wheel. It is found that when the radius is 12 mm, CGDI approaches a maximum value. When the inner diameter D of the pipeline is chosen as 100 mm, r is calculated as 12 mm, which is the optimal value. The pipeline robot was designed with this wheel parameter.

Fig. 12 shows the simulation result for (22). Fig. 12(a) shows the change in the joystick direction θ_J from $0°$ to $360°$. The vector $\underline{u}$ denotes the moving direction of the robot. For instance, if we want to turn left, then we steer the joystick to the left. In that case, wheel 1 is stationary, wheel 2 rotates to the positive direction, and wheel 3 rotates in the negative direction. Video clip 2 shows the motion of the three wheels according to the orientation of the joystick. Fig. 12(b) shows two history of the three wheels' angular velocity with respect to the angle θ_J, when ω_x and v_{cz} are given as 15 $°/\text{s}$ and 3 cm/s, respectively.
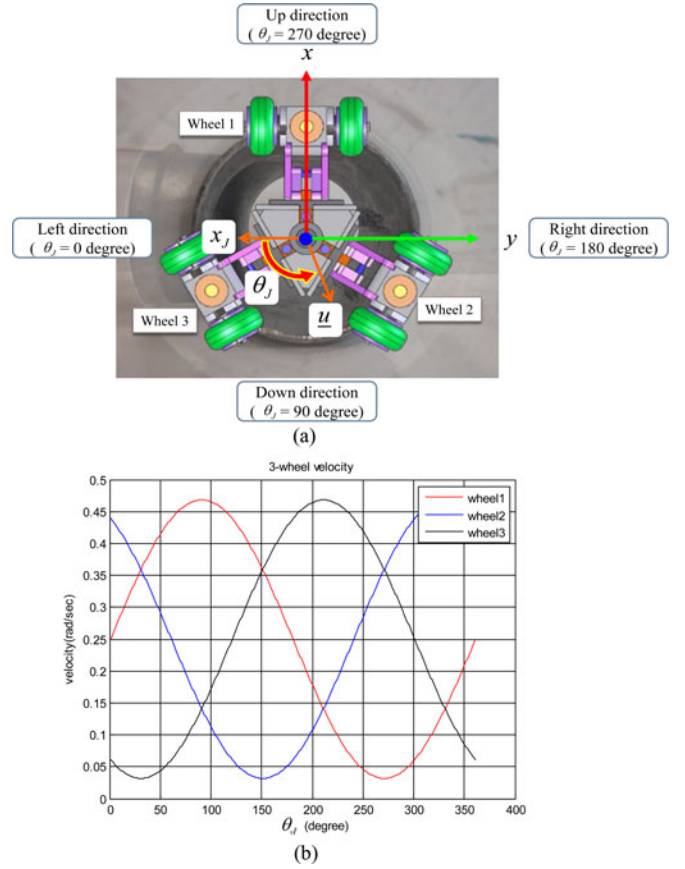
V. ACTUATOR SIZING

The folding linkage structure can be represented as Fig. 13. This is a four-bar mechanism, which consists of three revolute joints and one prismatic joint, as depicted. In order to determine the actuator size, it is necessary to perform static analysis. In Fig. 13, F_{Cx} and F_{Cz}, respectively, denote the reaction force and the normal force exerted on the four bars by the driving wheel. It is noted that only those forces conduct work. Applying the virtual work principle to the free-body diagram of Fig. 13 gives

$$\delta W = -F_{Cz}\delta z + F_{Bx}\delta x = 0 \tag{27}$$

where F_{Bx} is the compression force of the spring.

The corresponding displacements of those forces are expressed as

$$z = 2l\sin\psi, \quad x = -2l\cos\psi. \tag{28}$$

Substituting (28) into (27) yields

$$\delta W = -F_{Cz}\delta(2l\sin\psi) + F_{Bx}\delta(-2l\cos\psi)$$
$$= (-F_{Cz}2l\cos\psi + F_{Bx}2l\sin\psi)\delta\psi = 0. \tag{29}$$

Rearranging (29), the spring force F_{Bx} at the prismatic joint B is related to the normal force F_{Cz} by

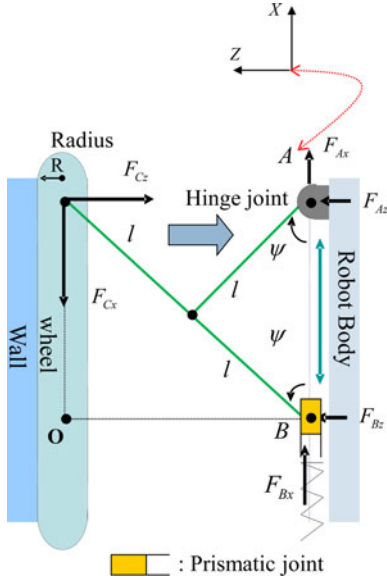$$F_{Cz} = F_{Bx}\tan\psi. \tag{30}$$

Fig. 13. Foldable linkage structure.

Fig. 14. Compression spring selecting table (folding mechanism).

In (30), the spring for F_{Bx} is equal to $k\Delta x_{Bx}$, where k and Δx_{Bx} denote the spring constant and the deflection of the spring, respectively.

Applying the static force equilibrium to the foldable four-bar mechanism, we have

$$\sum F_z = -F_{Cz} + F_{Az} + F_{Bz} = 0 \qquad (31)$$

$$\sum F_x = -F_{Cx} + F_{Bx} + F_{Ax} = 0 \qquad (32)$$

and

$$\sum M_A = 2F_{Cx}l\sin\psi - 2F_{Bz}l\cos\psi = 0. \qquad (33)$$

Using (31)–(33), the reaction forces F_{Bz}, F_{Ax}, and F_{Az} are found as

$$F_{Bz} = \frac{W}{3}\tan\psi, \quad F_{Ax} = \frac{W}{3} - F_{Bx},$$

$$F_{Az} = \left(F_{Bx} - \frac{W}{3}\right)\tan\psi. \qquad (34)$$

where W is the total weight of the robot.

From the aforementioned static analysis, it is found that the reaction force F_{Cz} is supported by the spring force [see (30)] and that the large weight W of the robot is structurally supported at the main body of the mechanism [see (34)] and does not influence the foldable motion of the linkage. It is noted that the reaction force F_{Cz} at the platform and the reaction forces F_{Ax}, F_{Az} at the body frame are a function of the spring force F_{Bx}. Thus, in the static case, the friction force $F_{Cx} = \mu F_{Cz}$ should be greater than $W/3$ to avoid slip. However, if F_{Cz} is too big, the wheel mechanism cannot move smoothly because of high friction forces. Therefore, the stiffness of the compression spring attached to the B position should be optimized.

We select the compression spring by considering three factors. First, it should be compressed enough to be inserted into the main body or enough for the four-bar mechanism to be folded.
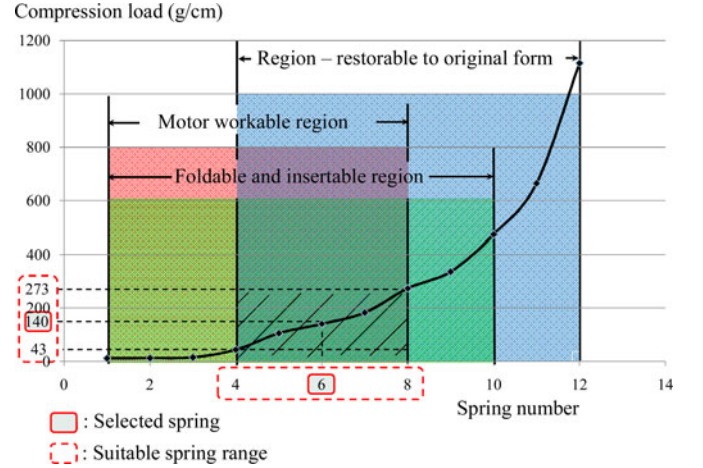
The foldable and insertable region in Fig. 14 corresponds to this case. The horizontal axis in Fig. 14 denotes 12 kinds of spring. A large number denotes a spring with high stiffness. Second, the compression force should not exceed the maximum motor torque, because a high compression force causes a high friction force on the wall. The motor workable region in Fig. 14 corresponds to this case. Third, the compression spring should restore to its original length when unfolding the configuration of the four-bar mechanism. The region—restorable to its original form—in Fig. 14 corresponds to this case. In Fig. 14, a common region that satisfies the three conditions ranges from spring numbers of 4 to 8. Among them, a spring of number 6, with a stiffness of 140 g/cm, is chosen for our design.

When the robot is moving vertically, w_1, w_2, and w_3 denote the traction forces exerted on the silicon belt by the wall of the pipeline. Assuming that they are the same, each reaction force F_{Cx} at the body is one-third of the total weight of the robot structure. It is the same as the traction force. Thus, the minimum torque capability of the actuator enclosed in the wheel is calculated by

$$\tau = F_{Cx}r = \frac{Wr}{3} \qquad (35)$$

where r is the radius of the caterpillar wheel.

Based on the specification of the robot given in Table I and the optimal radius of the wheel, the motor size is calculated as $\tau = 10.46$ mN · m. Thus, we select the motor, as shown in Table II. Considering the gear reduction, the output torque is calculated as 42.72 mN·m. Thus, the safety factor is 4.1 since the safety factor of 4+ is a good point to make robot at the motor selection step. It is also noted that the selected motor exceeds both the actuator load and the speed given in the specification of the wheel mechanism (see Table I).

VI. TWO-MODULE SYSTEM

A. Experimental Environment

We performed an experiment in an acrylic pipeline with an in-side diameter of 90 mm where the robot goes through an 80 mm

TABLE II
SPECIFICATION OF THE MOTOR (MAXON RE10) AND THE GEARHEAD (GP 10)

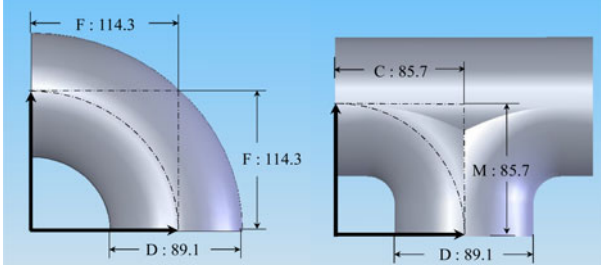| Specification	Value
Diameter	10 mm
Voltage	12 v
Linear speed	2790 rpm = 5.5 cm/s
Torque	0.741 mNm
Current	0.081 A
Gearhead reduction	64:1
Gearhead max. Continuous torque	100 mNm

Fig. 15. Elbow and the T-branch: (a) Cast iron elbow and (b) cast iron T-branch.

TABLE III
TYPES OF MOTION

Pipe type	T-branch		Elbow
direction	Motion 1	Motion 2	
Horizontal ⬇ Horizontal			
Horizontal ⬇ Vertical			
Vertical ⬇ Horizontal			
Vertical ⬇ Manifold			

Fig. 16. Experimental environment.

Fig. 17. Motion singularity. (a) Successful motion. (b) Singular position.

inside diameter pipeline that have multiple cast iron elbows and T-branches. The radius of curvature of the elbow is 114 mm and that of the T-branch is 86 mm, as shown in Fig. 15. This pipeline is used in standard pipes, and it corresponds to pipeline type 80 in Korea and Japan.

First, we checkthe motion capability at the elbow and the T-branch. There are three types of motion at the elbow and 16 types at the T-branch, as shown in Table III. The experimental environment was constructed by assembling three T-branches and one elbow, as shown in Fig. 16.
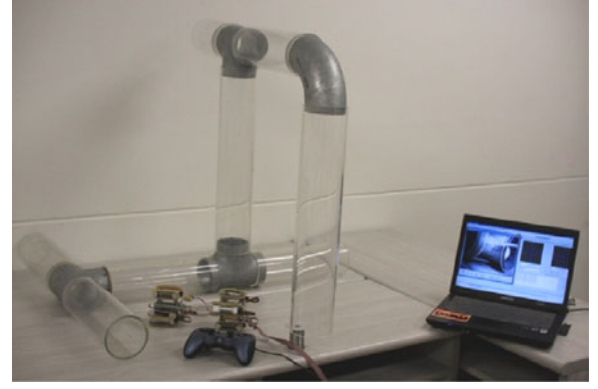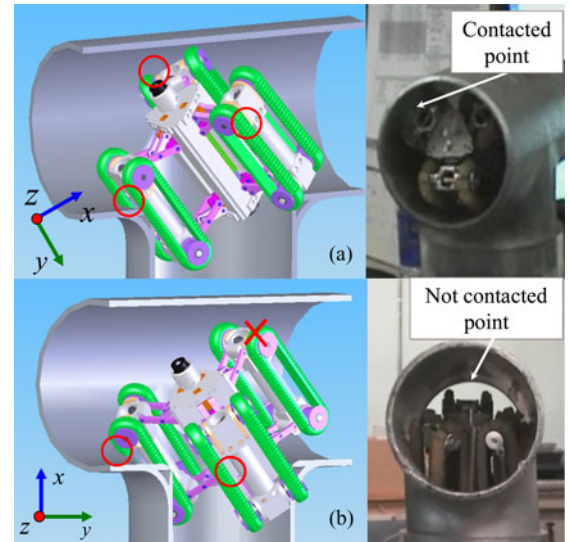
B. Problem of One-Module Experiment

When only one robot module is employed, there is a successful motion of going through a T-branch as shown in Fig. 17(a). However, sometimes the robot does not go through the T-branch, as shown in Fig. 17(b). This case happens when one caterpillar wheel loses contact at the turning position. This case is called "motion singularity." On the other hand, the robot is able to turn successfully if the two caterpillar wheels contact the outer surface of the pipeline, as shown in Fig. 17(a). Video clip 3 shows this phenomenon.

C. Collaboration of Two Robot Modules

To cope with such a motion singularity problem, we employ a spring for collaboration between two robot modules, as shown in Fig. 18.

The two modules are connected by a compression spring. The spring promotes smooth steering at the elbow or T-branch. Fig. 18 shows that the rear module is rotated 60° relative to the front module. This arrangement greatly helps to avoid motion singularity. Even though the front module confronts motion
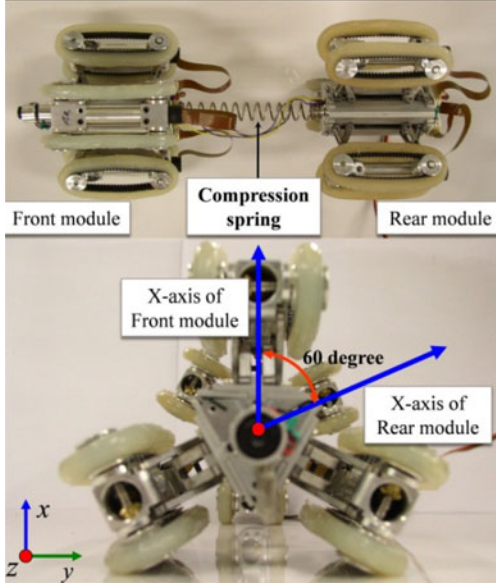
Fig. 18.   Collaborative structure between two modules constructed by using a compression spring.

Fig. 19.   Compression spring selection table (co-work mechanism).

singularity, the front module is able to pass through the elbow by the pushing force of the rear module. On the other hand, if the front module is able to go through the elbow, the front module pulls the rear module even though the motion singularity happens in the rear module. Here, the pushing–pulling force that is generated by the compression spring promotes successful steering at the elbow or T-branch.

The length of the spring is chosen as follows. The minimum radius of curvature of the spring can be found by a geometric analysis so that the two modules do not interfere with one another. Thus, the initial length L_s of the spring is calculated as

$$L_s = 2\pi R_s \times \left(\frac{\theta}{360} \right)$$
$$= 2 \times 3.14 \times 44 \times 0.25 = 69 \, \text{mm} \qquad (36)$$

where θ denotes the angle change of the elbow, and R_s denotes the radius of curvature of the spring. In practice, considering the part interfacing with each robot module, the length of the spring is set as 80 mm. We select the compression spring by considering two factors. First, it has to bend enough to pass through an elbow or T-branch. The bendable region in Fig. 19 corresponds to this case. Similar to Fig. 14, the horizontal axis in Fig. 19 denotes ten kinds of spring. A large number denotes a spring with high stiffness. Second, the compression spring has to be compliant enough to be restored to its original configuration after passing through an elbow or T-branch. The region—restorable to original form—in Fig. 19 corresponds to this case. In Fig. 19, a common region that satisfies the two conditions ranges from the spring number 5 to 8. Among them, the spring with number 7 whose stiffness is 556 g/cm was chosen for our design.
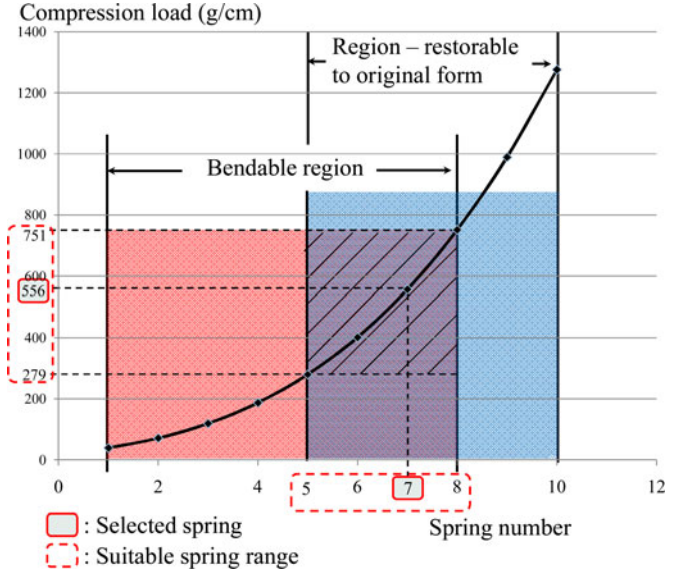
D. Motion Planning at Elbow

Fig. 20 shows the motion planning of the robot at an elbow. In the straight path, the speed of the two robot modules is identical. Thus, the spring that connect two modules is not compressed or elongated. However, as the front module enters the elbow, the speed of the front module is a little slower than that of the rear module. Then, the spring is compressed. Resultantly, the rear module pushes the front module so that the front module can go through the elbow effectively.

E. Motion Planning at T-Branch

Two solutions are proposed for the motion planning at the T-branch. One is active steering and the other is passive steering. Roh and colleagues [15] proposed an actively steerable in-pipe robot in which a 2-DOF steering mechanism was employed. However, active steering, it is expensive and bulky. In this study, we employ a passive steering method by arranging two modules connected by a compression spring.

Fig. 21 shows the motion planning of the robot at the T-branch from the horizon to the upward vertical pathway. The following summarizes the motion planning at the T-branch.
1) In the straight path
   a) the speed of the two robot modules is identical.
2) When the front module enters the T-branch
   a) the speed of the front module is planned to be a little slower than that of the rear module;
   b) the rear module pushes the front module so that it can go through the T-branch effectively.
3) At the exit of the T-branch
   a) the front module is a little faster than the rear module;
   b) the front module pulls the rear module so that the rear module can pass the T-branch successfully.

Video clip 4 demonstrates the corresponding experimental result. The front module makes a right turn. It is observed,
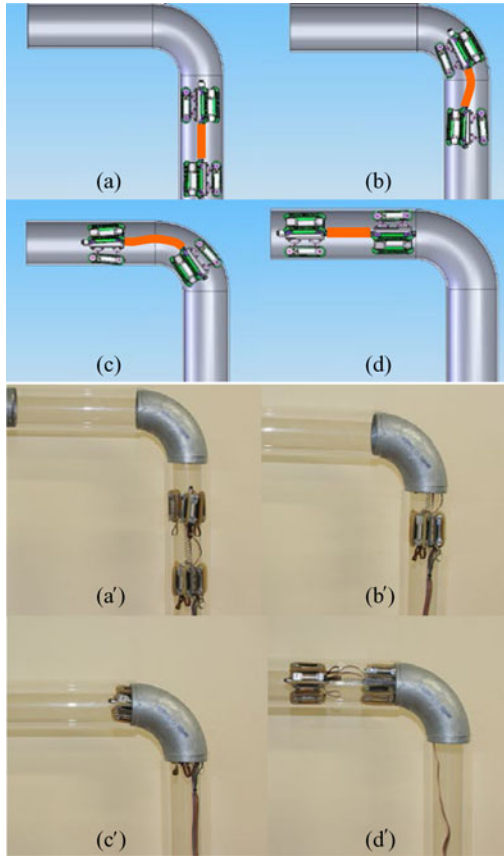
Fig. 20. Motion planning at the elbow. (a), (a′) Vertical path; (b), (b′) the front module steers to the left; (c), (c′) the rear module pushes the front module; and (d), (d′) the front module pulls the rear module.

Fig. 21. Co-work scenario. (a), (a′) straight path; (b), (b′) the front module steers to the left; (c), (c′) the front module hits the top of the pipeline; (d), (d′) the rear module pushes the front module; (e), (e′) and (f), (f′) the front module steps onto the left pathway; (g), (g′) and (h), (h′) the front module pulls the rear module; and (i), (i′) horizontal path.

through collaboration of the two modules, that the robot can go through the T-branch successfully with no motion singularity.

F. Most Difficult Problem at T-Branch

Motion planning at the T-branch is complicated, since there are many paths at the T-branch. By experience, the transition from the horizontal to the upward vertical pathway is found to be the most difficult task. This is because in this specific path of the T-branch, sometimes there is not much area for the front module wheels to grip the wall of the pipeline. The direction of the gravity load hinders the rotation from the horizon to the upward vertical direction. Most previous pipeline robots have had this difficulty. In order to increase the success rate in the vertical motion, the weight of the robot should be minimized and the traction force of the wheel part should be maximized. The mechanism is designed compactly to minimize the weight. Using the caterpillar wheel, the proposed robot system is able to overcome this difficulty by employing the caterpillar wheel instead of a rotating wheel, because the caterpillar wheel grasps relatively more contact area and the traction force of the silicon-covered wheel is also greater, as compared with the usual rolling wheel with one point of contact.
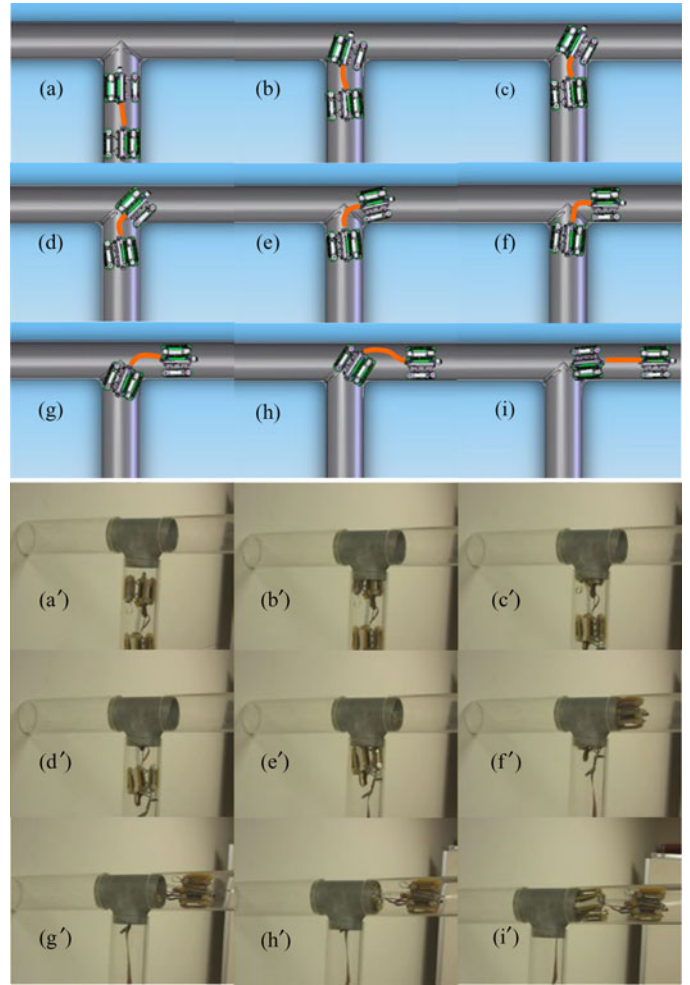
Fig. 22 shows that three wheels keep contacting the wall at the T-branch. The circled parts denote the contact areas of the caterpillar wheels on the wall of the T-branch.

In this case, the robot can go through the T-branch just by using the power of the front robot module. However, if a motion singularity similar to Fig. 17 happens, the transition from the horizontal pathway to the vertical pathway is still a difficult task. This is due to the arrangement of wheel chains, as shown in Fig. 23. Moreover, the gravity load that hinders the rising up of the robot module makes the situation much harder than that in Fig. 17. However, using two robot modules could resolve such a problem.

In the case that the front module loses contact with the wall, as shown in Fig. 23, the robot can be controlled by using collaboration between two robot modules, as explained in Section VI-C. In the process shown in Fig. 24(b)–(d), the compression force of the spring created by the rear robot pushes the front robot. It assists the turning motion of the front robot. In the process shown in Fig. 24(e)–(g), the front robot pulls the following robot
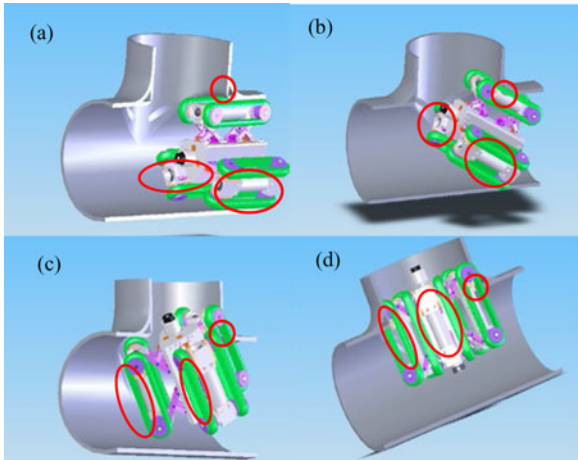
Fig. 22. Contact configuration at a T-branch (two outer wheels keep contact).
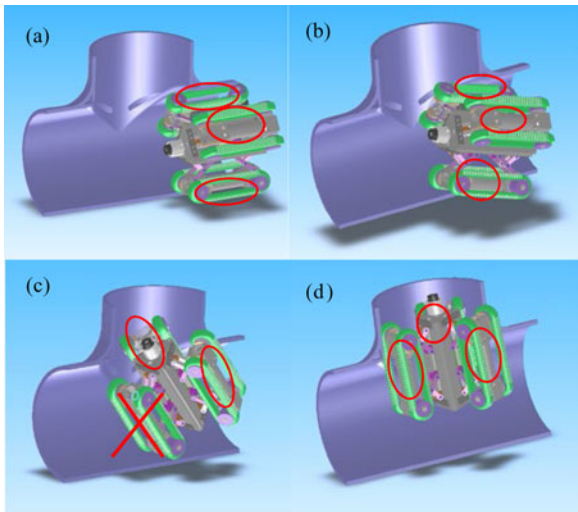

Fig. 23. Contact configuration at a T-branch (one outer wheel chain loses contact).

so that it can go through the T-branch smoothly. Conclusively, the spring also plays an important role in the motion planning of the robot at the T-branch. Video clip 5 clearly describes the motion at the T-branch. This video is taken inside the pipeline to show the collaboration between two robot modules.

VII. IMPLEMENTATION

A. Hardware Architecture

An effort was made to minimize the size of the robot system. A microcontroller was designed to be small enough to install inside the robot body. In addition, a sensor unit [16], which contains a dual-axis accelerometer and a single-axis gyro sensor unit, is designed for map building of pipelines. The traveling distance is measured by the encoder in the motor used to drive each wheel. The sensor unit plays the role of identifying the rolling angle of the robot body inside the pipeline. In the horizontal plane, the rolling angle can be calculated by the information of the dual-axis accelerometer. However, in the vertical pathway of
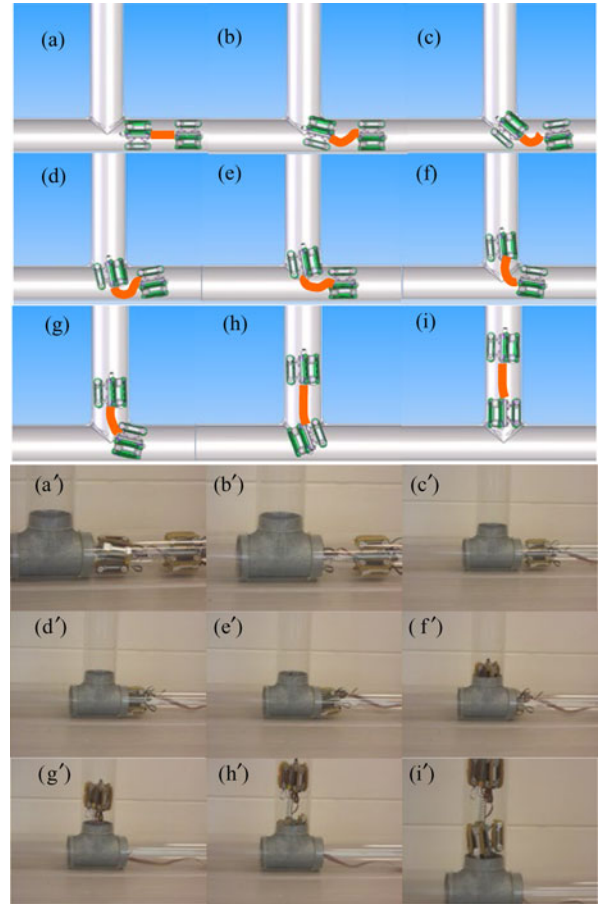

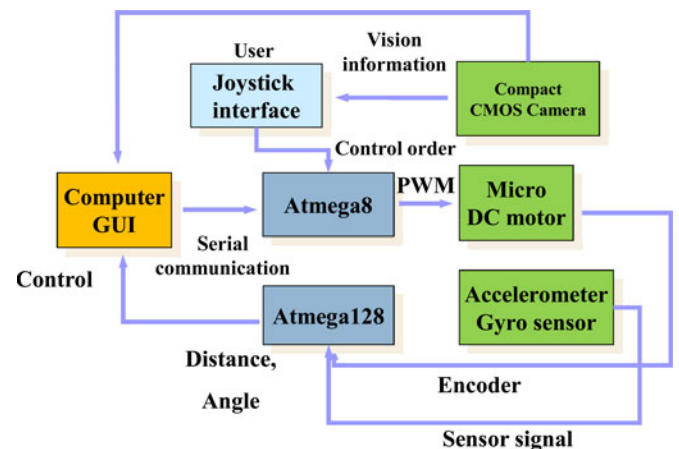Fig. 24. Motion planning at the T-branch for the case in Fig. 25.

Fig. 25. Flow chart of the robot system.

the robot, the gyro sensor measures the rolling angle by placing it parallel to the gravity direction.

Fig. 25 shows the system flow chart. When the order of the device control is given by the PC's graphic user interface (GUI), it is transferred to the robot by serial communication. Atmega8 controls motors and then Atmega128 returns sensor data for display on the GUI.
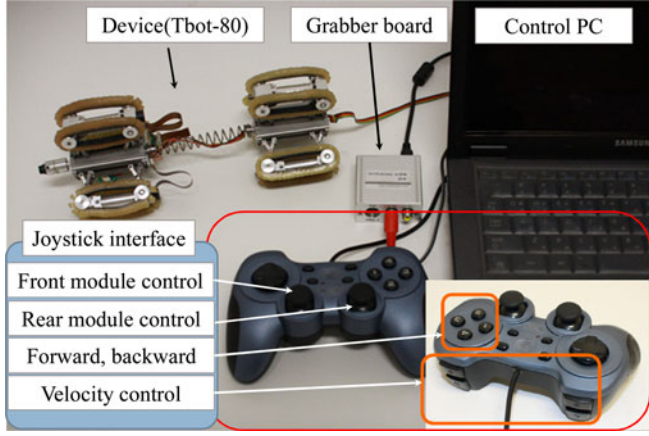
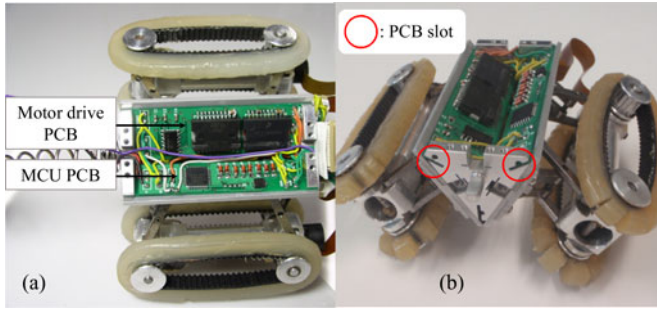Fig. 26. Components of the pipeline inspection robot.

Fig. 27. Motor control module. (a) Top view of the main body. (b) Front view of the main body and the PCB slots.

Fig. 28. Micro-CMOS camera and sensors.

Fig. 29. Sensor process module (the bottom view of the main body).

Users use the vision information from the GUI environment to control the robot. The two-axis accelerometer is used to locate the robot with respect to the global reference coordinate while moving inside the pipeline, whereas the gyro sensor is used to measure the rotation of the robot when it goes through a curved path.

Fig. 26 shows the entire picture of the pipeline inspection robot system. It is mainly divided into two parts: a robot device and a control system (power link circuit, control PC, grabber board, and a joystick interface). The control PC is a means of GUI, the robot-embedded part contains many sensors and processors for controlling the robot, and the grabber board transfers the signal of a micro-CMOS camera to the PC. The main body contains a main board consisting of an multipoint control unit (MCU) printed circuit board (PCB) (Atmega8), a motor drive PCB, and a sensor processor (AVR, Atmega128). Each linkage structure connects the main body to each caterpillar wheel.

The robot control is completed by serial communication. When a motion command is given by the GUI control panel, Atmega8 controls the motor's speed by producing a pulsewidth modulation signal. It can control all of the micro-dc motors and measure the displacement of the robot by the encoder. The main body has two PCB slots. The motor drive PCB and MCU PCB are embedded in the main body of the robot, as shown in Fig. 27.

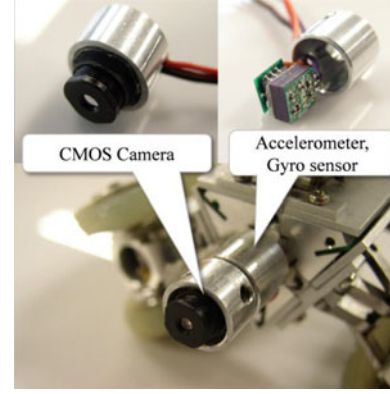Fig. 28 shows the minimized modularization of a micro-CMOS Camera and sensors. The module consists of a micro-CMOS Camera, a two-axis accelerometer, and a gyro sensor that is 12 mm in diameter and 20 mm in length.
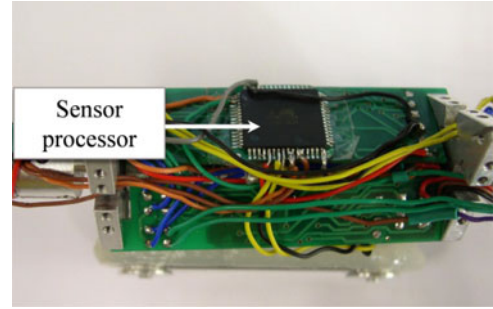
The view of the pipeline is provided to the user by using a micro-CMOS camera. The micro-CMOS camera is installed at the front module for inspection. This module makes it possible to inspect the condition inside the pipeline.

Fig. 29 shows a sensor processor module in which Atmega128 is installed. The processor calculates the displacement and rotation of the robot by using the sensor signals from a two-axis accelerometer, a gyro sensor, and an encoder of the micro-dc motor. The measured values are transferred to the PC.

B. Control Process

Users choose the steering direction from the camera view. Fig. 30(a) shows a global view of the pipeline environment. Fig. 30(b) and (c) shows the camera view coordinate and the joystick coordinate, respectively. The joystick has two handles: one for the front robot module and the other for the rear robot module. The robot modules can be controlled independently by the user. The joystick coordinate is matched to the camera view coordinate to control the steering direction. If the robot is going to turn to the left, then the user steers the joystick to the left.

First, the user decides the steering direction based on the camera view. Then, the user controls the steering direction using the joystick. The linear velocity is given a constant value and the angular velocity v_{cz} of the robot is decided according to

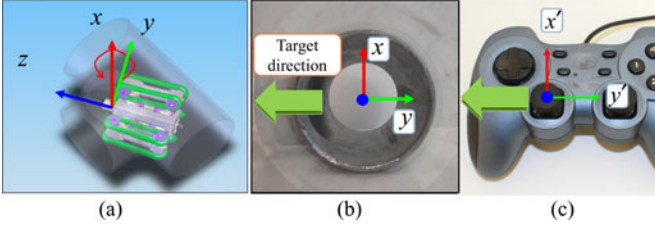$$\omega = \frac{v_{cz}}{\rho} \tag{37}$$

Fig. 30. Coordinate matching. (a) Global view. (b) User's camera view. (c) Coordinate of joystick.
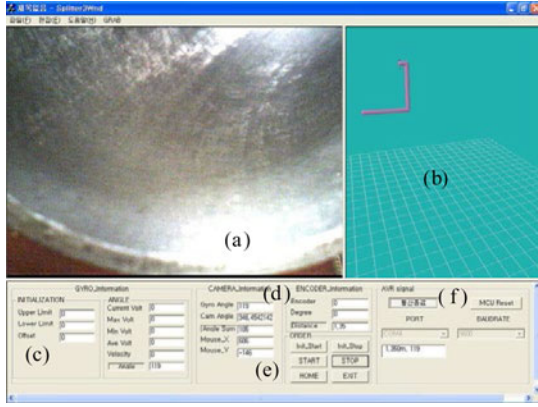

Fig. 31. Graphic user interface. (a) Micro-CMOS camera view. (b) Map view. (c) Device orientation information. (d) Distance information. (e) Control button. (f) Serial communication view.

where ρ is the radius of curvature, and $\omega = \sqrt{\omega_x^2 + \omega_y^2}$.

Then, a microprocessor (Atmega128) calculates the inverse Jacobian of (22). The result of this calculation is the angular velocity of each wheel.

C. Graphic User Interface

We run the robot using the GUI environment after opening a signal port. The GUI makes it possible to view the condition of the pipeline by using a micro-CMOS camera. The user checks how much the device has advanced from the origin of the global reference coordinate by using the encoder information from the motors. Using the information from the sensors, a map of the pipeline can be built, as shown in Fig. 31 (see [16] for details of the map-building algorithm). Autonomous navigation using sensor data will be also one of current research topics [23], [24].

VIII. EXPERIMENTAL RESULTS

A pipeline consisting of three T-branches and one elbow was employed in this experiment. The radius of curvature of the elbow is 114 mm and that of the T-branch is 86 mm. The maximum velocity of the robot is 9 cm/s, but in the experiment, we control the robot's velocity between 0 and 7 cm/s for safety.

We have two joystick control strategies: dependent mode and independent mode. In the straight pipeline, the two modules are controlled so as to have a common linear velocity. In the curved sections, the front and rear modules are controlled inde-

TABLE IV
TYPE OF MOTION AT THE ELBOW

TABLE V
TYPE OF MOTION AT THE T-BRANCH

pendently according to the motion planning algorithm given in Section VI. When the robot arrives at the entrance of a T-branch, the operator stops the robot motion and steers the motion direction of the front robot module with the joystick. Next, a command is sent to the rear robot module, such that the front module can pass through the T-branch using the pushing force of the rear module. Buttons that are available at the joystick are employed for those commands.

Table IV shows that the pipeline inspection robot is climbing up and down a vertical pipeline at the elbow. Table V shows that the pipeline inspection robot is turning in several directions in a T-branch of the pipeline. The performance of the two-module pipeline inspection robot was verified through experimentation. The attached video clip 6 includes the whole motion inside the pipeline. Sometimes, we experience failure because of moisture

inside the pipeline. Usually, pipelines are wet, and thus, the electronic systems might be damaged by water. To cope with this problem, the pipeline should be dried before inserting robots into pipelines. Currently, dust, cracks, or water in pipelines are removed by blowing a high-speed vortex flow along with some tiny sand particles. Finally, a robot is inserted into the pipeline for inspection. Water proofing the design of the pipeline robot should be accomplished as a future works.

In normal pipeline conditions with no moisture, the probability of success is almost 100%, although execution time of the planning algorithm differs (ranging from 20 to 70 s) according to the shape and condition of the T-branch.

A static force analysis was performed for actuator sizing in Section V. However, in the experiment, the actuator power is just enough to pass through the T-branch, even though we designed the safety factor to be 4.1. This is because there are some factors that we did not consider: friction between parts, the characteristics of the silicon belt, the friction of the bevel gear, and so on. Thus, the caterpillar type consumes more energy compared with other wheel types. In future work, in order to resolve this problem, more effort should be made to minimize the friction by improving manufacturing accuracy and selecting better material for parts.

In this study, we only used one camera in the front robot. However, if we have an additional camera in front of the rear robot module, it would have helped navigation. In the future, we will implement one more camera in order to provide better visual information to the operator.

Another future work is the retrieval function. Sometimes, the robot gets stuck inside the pipeline for various reasons. In these cases, the robot needs to be taken out of the pipeline by using some retrieval function. The concept of using a clutch is a good solution for realization of the retrieval function. There are two types of clutches: a mechanical clutch and a magnetic clutch. Usually, the mechanical clutch guarantees a strong friction force, but it is usually too large, too heavy, and has a complex structure. In contrast, the magnetic clutch is relatively small sized, light, and has a simple structure, but it has a limitation in power. Roh *et al.* [18] employed a magnetic brake to connect or disconnect power between the motor and the driving wheel mechanism. However, frequently, such magnetic-type clutch mechanisms are still too large and complex to apply to small-sized robots operating in pipes with less than 100-mm diameters. In addition, the magnetic type limited in firmness of gripping. Therefore, continuous effort to investigate a retrieval function, which is adequate to the real environment, is required.

IX. CONCLUSION

A two-module pipeline inspection robot has been developed that can inspect 80–100-mm pipelines. Each robot module consists of three pairs of CWCs, each of which is operated by a micro-dc motor. Independent control of the speed of each CWC allows steering capability through elbows or T-branches. Each CWC is foldable by using an embedded four-bar mechanism and a compression spring. This allows the robot to maintain contact and adjust to the inner wall of pipelines with an irregular cross-

sectional area. The best strength of CWCs is the large contact area for traction over irregular surfaces. They also overcome the sharp corners of branches and elbows.

The motion of this robot was equivalent to an omnidirectional mobile robot when steering at corners, such as an elbow or a T-branch. Based on this concept, we have derived a closed-form Jacobian of a pipeline inspection robot driven by three powered wheel chains. The analytic Jacobian is used to find the optimal value of the radius of the robot wheel.

Using a two-module robot connected by a compressive spring, the turning motion at both the elbow and T-branch can be conducted successively with no motion singularity. Motion planning with the assistance of a passive spring helps avoid the singular motion. The performance of the proposed pipeline inspection robot system was verified through a variety of experiments in a test-bed environment.

This study can be applied to design and control of pipeline inspection robots with diameters ranging from 40 mm to more than 100 mm.

APPENDIX

The ratio between the input velocity vector and the output velocity vector is expressed as [17]

$$\sigma_{\min} \|\dot{u}\| \leq \left\| \dot{\underline{\theta}}_a \right\| \leq \sigma_{\max} \|\dot{\underline{u}}\| . \tag{38}$$

The static force relation, which is dual to (17), is denoted as

$$\underline{\tau} = [G_a^u]^T \underline{f}, \tag{39}$$

where $\underline{\tau}$ and $\underline{f}$ denote the input torque vector and the operational force vector, respectively. Then, the ratio between $\underline{\tau}$ and $\underline{f}$ is expressed as

$$\frac{1}{\sigma_{\max}} \|\underline{\tau}\| \leq \|f\| \leq \frac{1}{\sigma_{\min}} \|\underline{\tau}\| . \tag{40}$$

REFERENCES

[1] T. Oya and T. Okada, "Development of a steerable, wheel-type, in-pipe robot and its path planning," *Adv. Robot.*, vol. 19, no. 6, pp. 635–650, 2005.
[2] S. Hirose, H. Ohno, T. Mitsui, and K. Suyama, "Design of in-pipe inspection vehicles for _25, _50, _150 pipes," in *Proc. IEEE Int. Conf. Robot. Autom.*, 1999, pp. 2309–2314.
[3] C. Jun, Z. Deng, and S. Y. Jiang, "Study of locomotion control characteristics for six wheels driven in-pipe robot," in *Proc. IEEE Int. Conf. Robot., Biomimetics*, 2004, pp. 119–124.
[4] S. G. Roh and H. Choi, "Differential-drive in-pipe robot for moving inside urban gas pipelines," *IEEE Trans. Robot.*, vol. 21, no. 1, pp. 1–17, Feb. 2005.
[5] T. Fukuda, H. Hosokai, and M. Uemura, "Rubber gas actuator driven by hydrogen storage alloy for in-pipe inspection mobile robot with flexible structure," in *Proc. IEEE Int. Conf. Robot. Autom.*, 1989, pp. 1847–1852.
[6] A. M. Bertetto and M. Ruggiu, "In-pipe inch-worm pneumatic flexible robot," in *Proc. IEEE/ASME Int. Conf. Adv. Intell. Mechatronics*, 2001, vol. 2, pp. 1226–1231.
[7] A. A. Transeth and K. Y. Pettersen, "Snake robot obstacle-aided locomotion: modeling, simulations, and experiments," *IEEE Trans. Robot.*, vol. 24, no. 1, pp. 88–104, Feb. 2008.
[8] A. Crespi and A. J. Ijespeert, "Online optimization of swimming and crawling in an amphibious snake robot," *IEEE Trans. Robot.*, vol. 24, no. 1, pp. 75–87, Feb. 2008.
[9] S. Hirose and H. Yamada, "Snake-like robots [Tutorial]," *IEEE Robot. Autom., Mag.*, vol. 16, no. 1, pp. 88–98, Mar. 2009.

[10] J. H. Kim, Design of a fully autonomous mobile pipeline exploration Robot (FAMPER) (2008). [Online]. Available: http://en.scientificcommons.org/38276528

[11] J. G. Park, T. H. Kim, and H. S. Yang, "Development of an actively adaptable in-pipe robot," in *Proc. IEEE Int. Conf. Mechatronics*, 2009, pp. 1–5.

[12] Raytheon. Multi-dimensional mobility robot (MDMR) (2012). [Online]. Available: http://www.raytheon.com/newsroom/technology/rtn09ausa/videos/index.html

[13] B. B. Gamble and R. M. Wiesman, "Tethered mouse system for inspection of gas distribution mains," *Gas Res. Inst.*, Doc. GRI-96/0209, 1996.

[14] C. Anthierens, C. Libersa, M. Touaibia, M. Betemps, M. Arsicault, and N. Chaillet, "Micro robots dedicated to small diameter canalization exploration," in *Proc. IEEE/RSJ Int. Conf. Intell. Robots Syst.*, 2000, pp. 480–485.

[15] S. M. Ryew, S. H. Baik, S. W. Ryu, K. M. Jung, S. G. Roh, and H. R. Choi, "Inpipe inspection robot system with active steering mechanism," in *Proc. IEEE/RSJ Int. Conf. Intell. Robots Syst.*, 2000, pp. 1652–1657.

[16] H. Lim, J. Y. Choi, Y. S. Kwon, E. J. Jung, and B.-J. YI, "SLAM in indoor pipelines with 15 mm diameter," in *Proc. IEEE Int. Conf. Robot. Autom.*, 2008, pp. 2616–1619.

[17] J. H. Lee, B.-J. Yi, S. R. Oh, and I. H. Suh, "Optimal design and development of a five-bar finger with redundant actuation," *Mechatronics*, vol. 11, no. 1, pp. 27–42, 2001.

[18] S. G. Roh, D. W. Kim, J. S. Lee, H. P. Moon, and H. R. Choi, "In-pipe robot based on selective drive mechanism," *Int. J. Control, Autom., Syst.*, vol. 7, pp. 105–112, 2009.

[19] H. Kimura, S. Hirose, and K. Shimizu, "Stuck evasion control for active-wheel passive-joint snake-like mobile robot 'Genbu'," in *Proc. IEEE Int. Conf. Robot. Autom.*, 2004, pp. 5087–5092.

[20] Y. Zhang, M. Zhang, H. Sun, and Q. Jia, "Design and motion analysis of a flexible squirm pipe robot," in *Proc. IEEE Int. Conf. Intell. Syst. Design Eng. Appl.*, 2010, pp. 527–531.

[21] A. Kuwada, Y. Adomi, K. Suzumori, T. Kanda, S. Wakimoto, and N. Kadowaki, "Snake-like robot negotiating three-dimensional pipelines," in *Proc. IEEE Int. Conf. Robot., Biomimetics*, 2007, pp. 989–994.

[22] Y. Kim and M. A. Minor, "Distributed kinematic motion control of multi-robot coordination subject to physical constraints," *Int. J. Robot. Res.*, vol. 26, no. 9, pp. 755–775, 2007.

[23] Y.-C. Chang and Y. Yamamoto, "Path planning of wheeled mobile robot with simultaneous free space locating capability," *J. Intell. Service Robot.*, vol. 2, no. 1, pp. 9–22, 2009.

[24] Y.-J. Lee and J.-B. Song, "Three-dimensional iterative closest point-based outdoor SLAM using terrain classification," *J. Intell. Service Robot.*, vol. 4, no. 2, pp. 147–158, 2011.
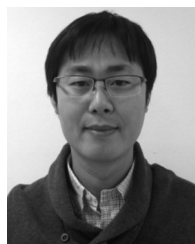
Young-Sik Kwon (M'10) received the B.Eng. and M.Eng. degrees from the Department of Electronic, Electrical, Control and Instrumentation Engineering, Hanyang University, Seoul, Korea, in 2006 and 2008, respectively, where he is currently working toward the Ph.D. degree with the Human-Robotics Laboratory.

His research interests include the pipeline inspection robot mechanism and surgical robot system.

Mr. Kwon is a Student Member of the IEEE Robotics and Automation Society.

Byung-Ju Yi (M'89) received the B.S. degree from Hanyang University, Seoul, Korea, in 1984, and the M.S. and Ph.D. degrees from the University of Texas at Austin, in 1986 and 1991, respectively, all in mechanical engineering.

From January 1991 to August 1992, he was a Postdoctoral Fellow with the Robotics Group, University of Texas at Austin. From September 1992 to February 1995, he was an Assistant Professor with the Department of Mechanical and Control Engineering, Korea Institute of Technology and Education, Chonan, Chungnam, Korea. In March 1995, he joined the Department of Control and Instrumentation Engineering, Hanyang University, where he is currently a Professor with the Department of Electronic Systems Engineering. He was a Visiting Professor with Johns Hopkins University, Baltimore, MD, in 2004 and a JSPS Fellow with the Kyushu University, Fukuoka, Japan, in 2011. His research interests include general robot mechanics with application to surgical robotic systems (ENT, Neurosurgical, and needle insertion areas), pipeline inspection robots, and ubiquitous sensor network-based robotics.

Dr. Yi is a member of the IEEE Robotics and Automation Society and has served as an Associate Editor of the IEEE TRANSACTIONS ON ROBOTICS from 2005 to 2008. He is currently a Board Member of the Korean Robotics Society and the Korean Society of Medical Robotics.